Received: 24 May 2023 | Revised: 3 October 2023 | Accepted: 14 December 2023

DOI: 10.1002/mp.16916

RESEARCH ARTICLE

MEDICAL PHYSICS

Out-of-field dosimetry using a validated PHITS model and computational phantom in clinical BNCT

Ryo Kakino[1] | **Naonori Hu**[1,2] | **Hiroki Tanaka**[2] | **Satoshi Takeno**[3] | **Teruhito Aihara**[1] | **Keiji Nihei**[1,3] | **Koji Ono**[1]

[1]Kansai BNCT Medical Center, Osaka Medical and Pharmaceutical University, Takatsuki, Osaka, Japan

[2]Institute for Integrated Radiation and Nuclear Science, Kyoto University, Osaka, Japan

[3]Department of Radiation Oncology, Osaka Medical and Pharmaceutical University, Takatsuki, Osaka, Japan

Correspondence
Naonori Hu, Kansai BNCT Medical Center, Osaka Medical and Pharmaceutical University, 2–7 Daigaku-machi, Takatsuki, Osaka, 569–8686, Japan.
Email: naonori.ko@ompu.ac.jp

Funding information
JSPS; Grant-in-Aid for Research Activity Start-up, Grant/Award Number: 21K20521; JSPS Grant-in-Aid for Scientific Research, Grant/Award Number: JP21K15793

Abstract

Background: The out-of-field radiation dose for boron neutron capture therapy (BNCT), which results from both neutrons and γ-rays, has not been extensively evaluated. To safely perform BNCT, the neutron and γ-ray distributions inside the treatment room and the whole-body dose should be evaluated during commissioning. Although, certain previous studies have evaluated the whole-body dose in the clinical research phase, no institution providing BNCT covered by health insurance has yet validated the neutron distribution inside the room and the whole-body dose.

Purpose: To validate the Monte Carlo model of the BNCT irradiation room extended for the whole-body region and evaluate organ-at-risk (OAR) doses using the validated model with a human-body phantom.

Methods: First, thermal neutron distribution inside the entire treatment room was measured by placing Au samples on the walls of the treatment room. Second, neutron and gamma-ray dose-rate distributions inside a human-body water phantom were measured. Both lying and sitting positions were considered. Bare Au, Au covered by Cd (Au+Cd), In, Al, and thermoluminescent dosimeters were arranged at 11 points corresponding to locations of the OARs inside the phantom. After the irradiation, γ-ray peaks emitted from the samples were measured by a high-purity germanium detector. The measured counts were converted to the reaction rate per unit charge of the sample. These measurements were compared with results of simulations performed with the Particle and Heavy Ion Transport code System (PHITS). A male adult mesh-type reference computational phantom was used to evaluate OAR doses in the whole-body region. The relative biological effectiveness (RBE)-weighted doses and dose-volume histograms (DVHs) for each OAR were evaluated. The median dose ($D_{50\%}$) and near-maximum dose ($D_{2\%}$) were evaluated for 14 OARs in a 1-h-irradiation process. The evaluated RBE-weighted doses were converted to equivalent doses in 2 Gy fractions.

Results: Experimental results within 60 cm from the irradiation center agreed with simulation results within the error bars except at $\pm$20, 30 cm, and those over 70 cm corresponded within one digit. The experimental results of reaction rates or γ-ray dose rate for lying and sitting positions agreed well with the simulation results within the error bars at 8, 4, 11, 7 and 7, 4, 7, 6, 5, 6 out of 11 points, respectively, for Au, Au+Cd, In, Al, and TLD. Among the detectors, the discrepancies in reaction rates between experiment and simulation were most common

for Au+Cd, but were observed randomly for measurement points (brain, lung, etc.). The experimental results of γ-ray dose rates were systematically lower than simulation results at abdomen and waist regions for both positions. Extending the PHITS model to the whole-body region resulted in higher doses for all OARs, especially 0.13 Gy-eq increase for $D_{50\%}$ of the left salivary gland.
Conclusion: The PHITS model for clinical BNCT for the whole-body region was validated, and the OAR doses were then evaluated. Clinicians and medical physicists should know that the out-of-field radiation increases the OAR dose in the whole-body region.

KEYWORDS
boron neutron capture therapy, Monte Carlo simulation, out-of-field dose, whole-body dose

1 | INTRODUCTION

Boron neutron capture therapy (BNCT) is a binary treatment that selectively kills tumor cells. During the neutron capture reaction with ^{10}B nuclei in boron compounds administrated to patients, two particles (α particle and ^{7}Li nuclei) with high linear energy transfers are generated. These particles cover a distance of 9 and 4 μm, which is smaller than the human-cell diameter.

Although conventional BNCT employed a nuclear reactor, current BNCT processes employ an accelerator owing to advantages such as the ease of installment at hospitals. The first accelerator-based neutron source for clinical BNCT was developed in collaboration by Sumitomo Heavy Industries, Ltd. and Kyoto University.[1,2] This system was installed at the Kansai BNCT Medical Center in Osaka Medical and Pharmaceutical University, as shown in Figure 1.[3] This system was tested through clinical trials and approved as a medical device for head and neck cancer by the Ministry of Health, Labor, and Welfare in March 2020.[4] Subsequently, BNCT for unresectable, locally advanced or recurrent carcinoma of the head and neck region has been approved for reimbursement under the national health insurance in June 2020. As of December 2022, more than 100 head and neck cancer patients have received BNCT.

One of the challenges experienced in BNCT is the lack of information available regarding the radiation exposed to the whole body. Imoto et al. conducted experiments and simulations to evaluate the neutron distribution inside the irradiation room, where the prototype of the BNCT system was installed.[5] Results revealed that there were unexpected neutrons that leaked from the gap between the neutron moderator and concrete wall. In addition, Tsukamoto et al. evaluated the whole-body dose using several water phantoms in the same prototype system, and found that the primary γ-rays and fast neutrons were dominant in the total exposure dose.[6] Based on these studies, to safely perform BNCT, the neutron and gamma-ray distributions inside the treatment room and the whole-body dose for

FIGURE 1 Neutron irradiation room equipped with a BNCT system (NeuCure) in Kansai BNCT Medical Center. BNCT, boron neutron capture therapy.

each BNCT system should be evaluated at the time of commissioning.

Herrera et al. evaluated the whole-body dose using the medical internal radiation dose phantom during the BNCT based on Tandem-ElectroStatic Quadrupole accelerator in Argentina. The results showed that the whole-body dose varied depending on the proximity of the neutron beam to the organs. Takada et al. evaluated the undesirable radiation dose based on the CT images of whole-body phantom during BNCT at Japan Research Reactor No. 4 in Japan. They showed that it is possible to simultaneously calculate not only treatment planning but also the dose at out-of-field. Postuma et al. aimed to design a clinical BNCT facility based on the Radio Frequency Quadrupole proton accelerator constructed by The Italian National Institute of Nuclear Physics, and performed treatment planning for head-and-neck cancer patients, and selected the optimal beam shaping assembly based on the results. Although, these previous studies have evaluated the whole-body dose in the clinical research phase,[7–9] no institution providing BNCT covered by health insurance has yet validated the whole-body dose. In addition, although the recommendation for the assessing and managing the out-of-field dose in external photon, electron, proton, carbon therapy, and brachytherapy has been published by the American Association of Physicists in Medicine report number 158, there is no recommendation of that for BNCT to date.[10]

In our previous study, we have developed a Monte Carlo model independent of the treatment planning system (TPS) for the clinical BNCT.[11] The size of the source was a radius of 30 cm which is within the treatment area of the BNCT. We validated the neutron flux and γ-ray dose rate inside a water phantom among the measurements, TPS, and the independent Monte Carlo model. The results closely matched within 5% for the thermal neutron flux and 10% for the γ-ray dose rate. However, our previous study did not consider the whole treatment room. Thus, there might be a possibility of whole-body radiation exposure from the out-of-field sources.

Hence, the objectives of this study are as follows:

1. To extend the source up to a radius of 150 cm and simulation region to cover the entire treatment room in the Monte Carlo model, which has been previously developed for the BNCT system,[11] and validate our simulated model by measuring neutrons and γ-rays outside the irradiation field by multiple activation foils and the thermoluminescent dosimeters (TLDs).
2. To evaluate organ-at-risk (OAR) doses using the validated Particle and Heavy Ion Transport code System (PHITS) model with a human-body phantom, for the whole-body dosimetry.

2 | METHODS

2.1 | Validation of the extended PHITS model

2.1.1 | Neutrons on the room wall

All experiments were performed using an accelerator-based BNCT system NeuCure (Sumitomo Heavy Industries, Ltd., Japan) installed at our institution. The room wall was mainly made with concrete, and polyethylene loaded with natural LiF (LiF-PE) was added near the proximity of the patient. A collimator with a 15-cm-diameter beam aperture (maximum diameter for insurance treatment) was used for neutron irradiation. A water phantom (H: 28 cm, L: 21 cm, W: 21 cm) was placed at the collimator surface for neutron thermalization. This phantom was frequently used in quality assurance (QA) measurement in our institution and was large enough not to affect the depth-thermal-neutron-flux profile along the central axis at the 15-cm beam aperture. The activation method of Au was adopted to measure neutrons inside the entire BNCT irradiation room. The Au-activation method is a useful method for neutron measurements in clinical BNCT as it has high sensitivity to both thermal and epi-thermal neutrons. Thin Au wires (0.25 mm diameter, which were cut into a small round piece beforehand), or Au foil (10 mm diameter, 0.05 mm thickness) (99.95% purity, The Nilaco Corporation, Tokyo, Japan) were attached on the wall of the collimator side at $\pm$20, $\pm$30, …, $\pm$100,$\pm$125,$\pm$150,$\pm$175,$\pm$200,$\pm$250, and $-$300 cm from the irradiation center. Au has a relatively large cross section for thermal neutrons, which decreases according to the 1/v law with higher neutron energies. Moreover, they were attached at three points on both the left and right sides and five points on the opposite side, viewed from the collimator side. The room geometry and arrangement of the Au wires or foils are illustrated in Figure 2. A proton charge of 3.6 C was delivered for the activation of Au samples. After the irradiation, 412 keV γ-rays emitted from ^{198}Au inside the activated Au samples were measured with a high-purity germanium (HPGe) detector (ORTEC ICS-P4). Then, the measured counts were converted to the reaction rate per unit charge of the Au sample. The details of the conversion are summarized in Appendix A. Conversely, the PHITS was used for the Monte Carlo simulation.[12] The PHITS model for the clinical BNCT in our institution had already been modeled and validated.[11] Although a planar neutron source was simulated with a radius of 30 cm from the irradiation center (referred as S_{30}) in our previous work, in this study, it was extended to a radius of 150 cm (referred as S_{150}) to evaluate whole-body dose evaluation. Moreover, opposite, left, and right sides of concrete walls were modeled, which were not considered in our

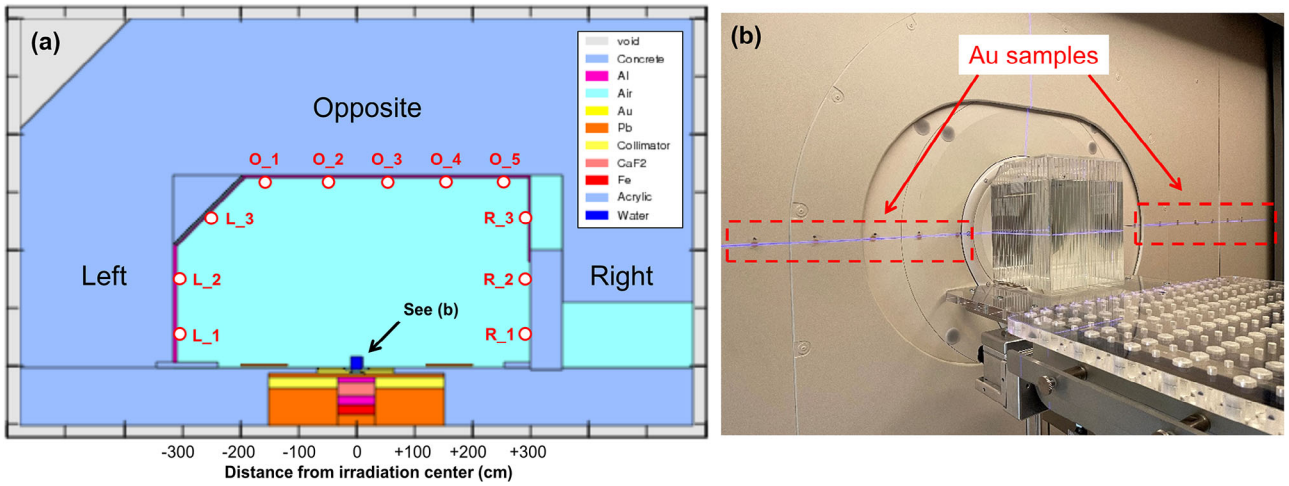

FIGURE 2 (a) Geometry of the irradiation room and the arrangement of the Au samples in the left, opposite, and right sides. (b) Photograph of the arrangement of the Au samples and the water phantom on the collimator side. A 15-cm φ beam aperture and a water phantom (H:28 cm, L: 21 cm, W: 21 cm) was used.

previous work. [T-track] function was used for the evaluation of the neutron spectrum inside the Au sample. The spectrum was multiplied by the neutron-reaction cross section (The Japanese Evaluated Nuclear Data Library 4.0) of Au using the [Multiplier] section to the evaluate the reaction rate. Subsequently, the calculated reaction rate was compared with experimental results.

2.1.2 | Neutrons and photons inside the whole-body water phantom

A human-body phantom was created by combining several rectangular water phantoms. The neutron reaction and γ-ray dose rates inside the phantom were evaluated for the validation of the whole-body dose. Both lying and sitting positions were considered, which were operated in clinical BNCT. Figure 3 shows the layout, experimental, and simulation geometries of the human-body phantom. Bare Au foil (with the same size as the previous section), Au foil sandwiched between two Cd foils (φ: 10 mm, T: 1.0 mm and referred as Au+Cd), In (φ: 20 mm, T: 0.5 mm), Al (φ: 20 mm, T: 2.5 mm) foils, and special-ordered TLDs of BeO powder enclosed in a quartz glass capsule[13] were arranged at 11 points corresponding to OARs inside the phantom (brain, thyroid, esophagus, bone marrow, lung, breast, stomach, liver, colon, and bladder). Cadmium foil absorbs neutrons below 0.5 eV. Thus, the Au+Cd detector reacts mainly to epi-thermal neutrons with the energy above 0.5 eV. These detectors correspond to measurements of thermal and epi-thermal neutrons, For In and Al foils, ^{155}In(n, n')^{155m}In and ^{27}Al(n, α)^{24}Na reactions were used to detect fast neutrons with the different threshold energy above 0.4 MeV[14] and 3.4 MeV. TLD measures γ-ray dose rate. The selection of OARs is partly based on the findings of Tsukamoto et al.[6] Fast neutrons had already been validated by Hu et al. using In samples at the center of the water phantom surface.[11,15] Here, an additional validation of fast neutrons in a different energy range using In and Al samples inside the water phantom was performed prior to the whole-body dose validation (see Appendix B). For the validation of the whole-body dose, the samples were separated into two groups to minimize measurement errors that may be caused by the neutron field disturbance; group 1 consisted of Au and TLD samples, and group 2 consisted of Au+Cd, In, and Al samples. Proton charges of 3.6 and 7.2 C were irradiated to groups 1 and 2, respectively. All group 2 samples were covered in a Cd case to reduce the difficulty of measuring the γ-ray peak of interest owing to unnecessary activation by thermal neutrons. After the irradiation, γ-ray peaks emitted from the samples (Au: 412 keV, In: 336 keV, Al: 1369 keV)[16,17] were measured by the HPGe detector, same as in the previous section. The details of the detection efficiency of the HPGe are discussed in Appendix A. The simulation procedure was the same as that in the previous section.

2.1.3 | Estimation of the whole-body dose using a computational phantom

The male-adult mesh-type reference computational phantom (MRCP) published by International Commission on Radiological Protection was used to evaluate OAR doses in the whole-body region. The mesh phantom can be modified to different postures. That is, it is expected to be useful in evaluating the effect of different postures for OAR doses in future. The relative biological effectiveness (RBE)-weighted doses and the

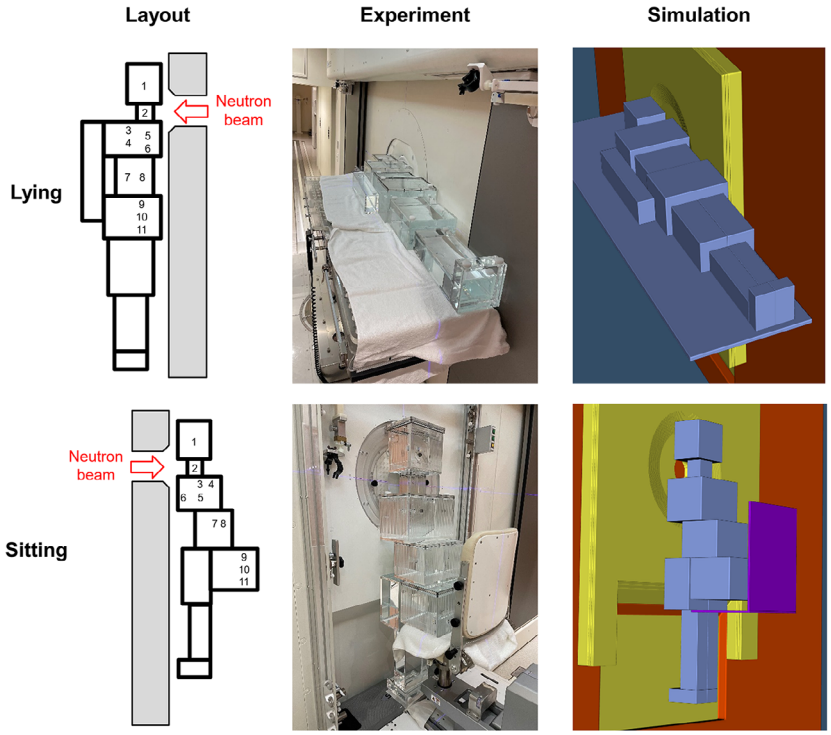

FIGURE 3 Arrangement of the whole-body phantom: layout, experiment, and simulation. The numbers indicate different measurement points as follows: 1, brain; 2, thyroid; 3, esophagus; 4, bone marrow; 5, lung; 6, breast; 7, stomach; 8, liver; 9, colon; and 10, bladder.

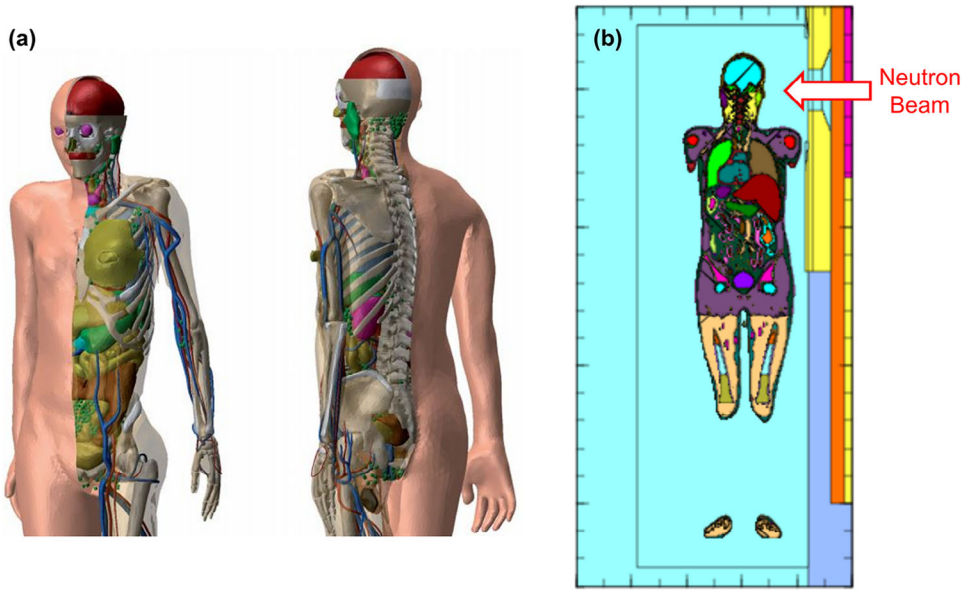

FIGURE 4 (a) Adult mesh-type reference computational phantom (MRCP). (b) MRCP arrangement in the validated PHITS model. MRCP, mesh-type reference computational phantom.

dose-volume histograms (DVHs) for each OAR were evaluated by calculating the physical dose for all tetra meshes inside the MRCP. The MRCP was arranged in the validated PHITS model, considering the lying position for treating the region around the ear canal, as shown in Figure 4. The equation used for dose calculations is summarized in Appendix C. The ^{10}B concentration in the blood was assumed to be 25.0 μg/g. The median dose ($D_{50\%}$) and near-maximum dose ($D_{2\%}$) in a 1-h-irradiation process were evaluated for 14 OARs (brain, left eye (Eye_L), right eye (Eye_R), left salivary gland (Salivary_L), right salivary gland (Salivary_R), thyroid, esophagus, spinal_cord, left lung (Lung_L), right lung (Lung_R), stomach, liver, rectum, bladder). The evaluated RBE-weighted doses were converted to an equivalent dose in 2 Gy fractions (EQD2)

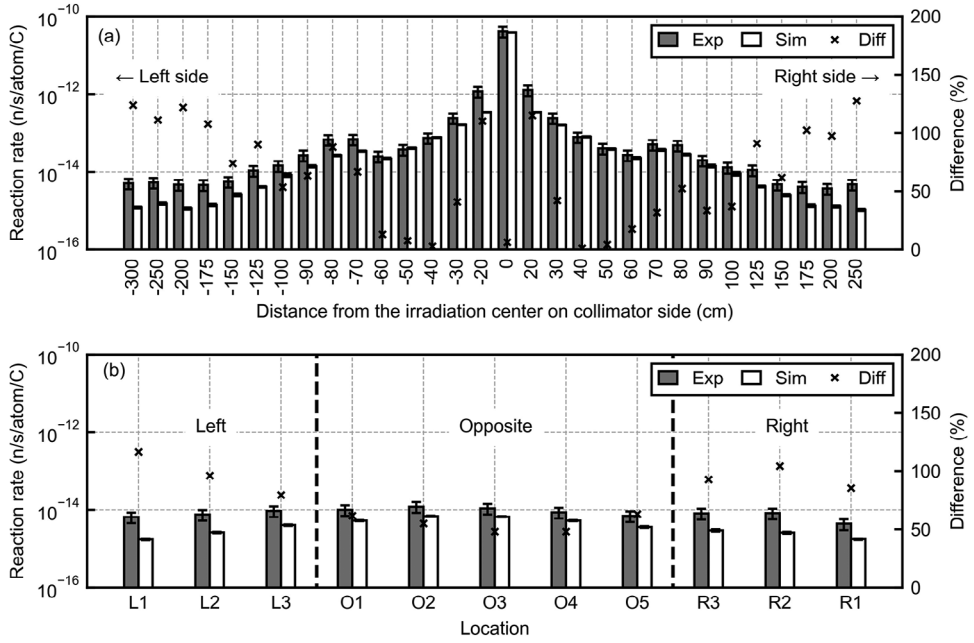

FIGURE 5 Comparison of reaction rates of the Au samples attached at (a) the collimator side and (b) left, opposite, and right sides. The error bars include several uncertainties such as statistical errors of the radiation measurement, efficiency calibration of the germanium detector, and positioning error of the detectors. Exp, experiment; Sim, simulation; Diff, difference.

using the following equation:

$$EQD2 = nd\left(\frac{d+\alpha/\beta}{2+\alpha/\beta}\right), \quad (1)$$

where n is the fraction number (= 1 for clinical BNCT), d is the dose per fraction, α/β denotes the dose where linear and quadratic components cause the same amount of cell killing (= 3 for normal tissues in this study). Moreover, EQD2 was compared with that evaluated using the conventional PHITS model with the S_{30} neutron source and without considering concrete walls, to confirm the usefulness of the extended PHITS model used in this study. Absolute error ε_a and relative error ε_r of the EQD2 values for S_{150} against those for S_{30}. referred as $EQD2_{S150}$ and $EQD2_{S30}$, respectively, were evaluated using the following equations:

$$\varepsilon_a = EQD2_{S150} - EQD2_{S30}, \quad (2)$$

$$\varepsilon_r = \frac{EQD2_{S150} - EQD2_{S30}}{EQD2_{S30}}. \quad (3)$$

In addition, internal doses due to radionuclides produced in the MRCP by the neutron irradiation were evaluated (see Appendix D).

3 | RESULTS

Figure 5a shows the reaction rates of Au attached on the wall of the collimator side. Experimental results of those within 60 cm from the irradiation center agreed well with the simulation results within the error bars, except points at ±20, 30 cm. Those over 70 cm from the irradiation center only corresponded within one digit. Figure 5b shows those attached on the wall of the left, opposite, and right sides. Those also agreed well within one digit. Figure 6 shows the reaction rates of activation foils and γ-ray dose rates arranged inside the whole-body phantom, and their ratios of sitting position to lying position. The experimental results of reaction rates or γ-ray dose rate for lying and sitting positions agreed well with the simulation results within the error bars at 8, 4, 11, 7 and 7, 4, 7, 6, 5, 6 out of 11 points, respectively, for Au, Au+Cd, In, Al, and TLD. The discrepancies in neutron reaction rates between the experiment and the simulation were observed most frequently for Au+Cd among the detectors and randomly for the measured points. The experimental results of γ-ray dose rates were systematically lower than simulation results at abdomen and waist regions for both lying and sitting positions. Figure 7 shows the comparison of DVHs evaluated via EQD2 of OARs between S_{30} and S_{150}. In addition, Table 1 shows $D_{50\%}$ and $D_{2\%}$ of EQD2, and their ε_r values. Table 2 shows the comparison of the obtained RBE-weighted doses (not EQD2) with those from previous research. These simulations had been conducted using phantoms in lying positions. The internal dose due to radionuclides produced in the MRCP by the neutron irradiation was sufficiently lower than the external dose such that it was considered negligible (Appendix D).

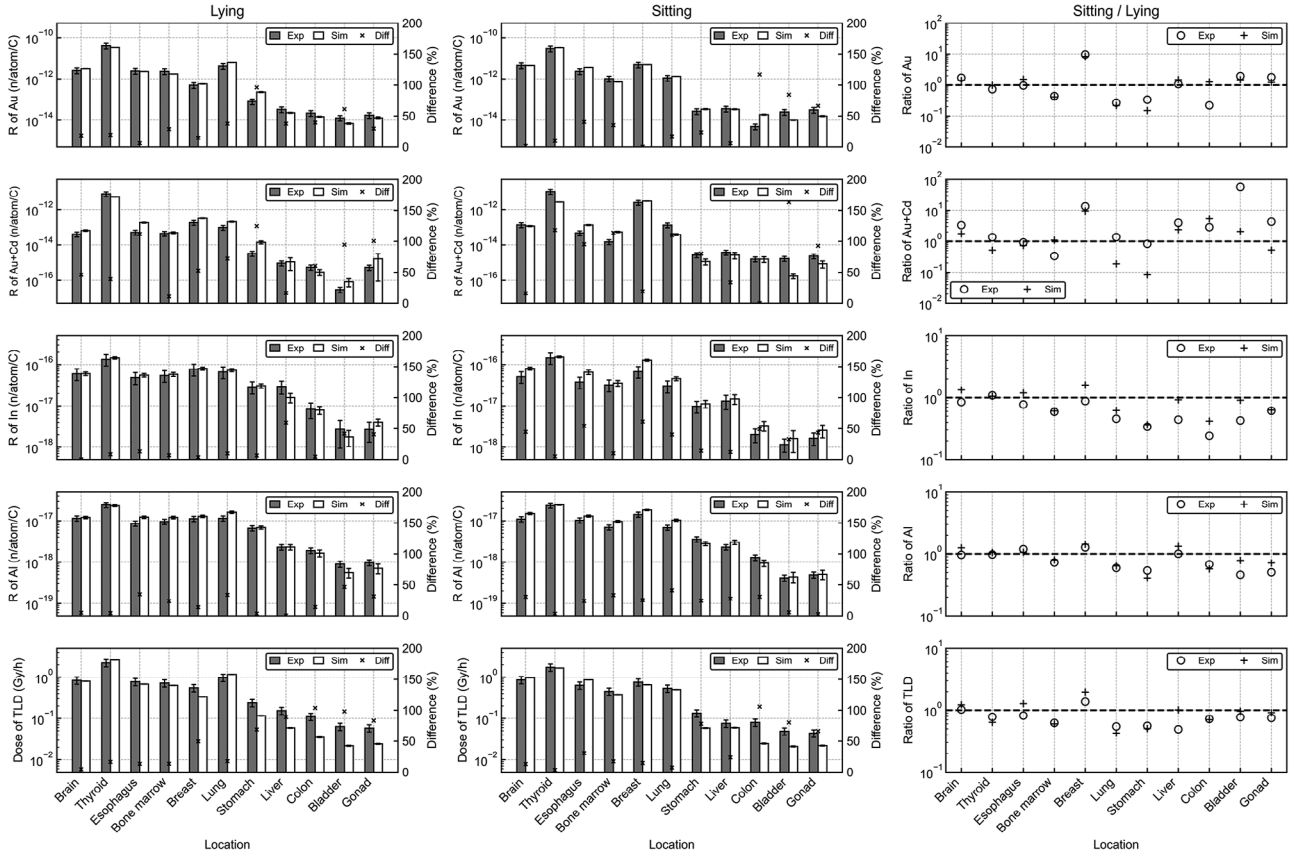

FIGURE 6 Reaction rates of activation samples or γ-ray dose rates in lying and sitting positions for validation in whole-body phantoms, and their ratios (sitting / lying). Exp, experiment; Sim, simulation; Diff, difference.

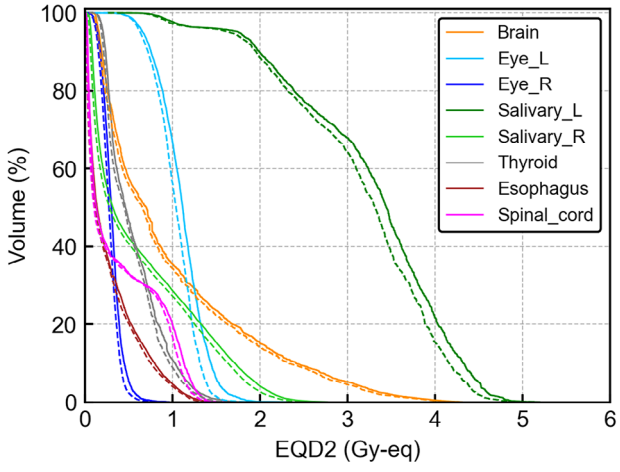

FIGURE 7 DVHs of OARs in EQD2. Solid lines represent DVHs for the whole-room PHITS model (S_{150}), and broken lines represent DVHs for the in-field PHITS model (S_{30}). DVH, dose-volume histogram; OAR, organ-at-risk; EQD2, equivalent doses in 2 Gy fractions; S_{150}, source within a radius of 150 cm; S_{30}, source within a radius of 30 cm.

4 | DISCUSSION

To the best of our knowledge, this is the first study to model the entire treatment room of a BNCT system that is, covered by insurance and evaluate whole-body doses using the MRCP. This study is unique because the results of whole-body doses were supported by the validations of the whole-room neutron distribution and thermal neutrons, epi-thermal neutrons, fast neutrons, and γ-ray dose rate inside the human-body water phantom. Furthermore, more OAR doses were evaluated in this study, compared to previous studies, and in addition to $D_{50\%}$ ($\approx D_{mean}$ in the previous studies), which was evaluated for parallel organs, $D_{2\%}$ was evaluated for serial organs. D_{mean} and D_{max} were not utilized in this study because of the unreliability at the arbitrary calculation points of the Monte Carlo simulation.[18]

Neutron measurements at the whole-room walls are useful for the validation of neutron distribution during BNCT. The unexpected neutron leakage can be determined by comparing neutron distributions obtained from measurements and simulations, as summarized by Imoto et al.[5] The other metal foils (Au+Cd, In, and Al foils) could not be adopted because their sensitivity was too low to validate the entire room. The TLDs also could not be adopted because of the limited number of the detectors in our institution. In this study, the reaction rates that were measured at two points, ±20 cm from the irradiation center on the collimator side, in the experiment were significantly higher than those from

TABLE 1 OAR doses ($D_{50\%}$ and $D_{2\%}$) in EQD2 for (a) whole-room and (b) in-field PHITS models.

OAR dose (Gy-eq)	$D_{50\%}$				$D_{2\%}$			
	S_{150}	S_{30}	ε_a	ε_r	S_{150}	S_{30}	ε_a	ε_r
Brain	0.70	0.66	0.04	0.07	3.51	3.38	0.13	0.04
Eye_L	1.12	1.04	0.08	0.07	1.66	1.46	0.20	0.13
Eye_R	0.30	0.27	0.03	0.10	0.59	0.52	0.07	0.13
Salivary_gland_L	3.44	3.32	0.13	0.04	4.63	4.49	0.14	0.03
Salivary_gland_R	0.32	0.28	0.04	0.14	2.17	2.07	0.10	0.05
Thyroid	0.46	0.45	0.01	0.03	1.35	1.28	0.07	0.06
Esophagus	0.14	0.11	0.03	0.23	1.15	1.13	0.02	0.02
Spinal_cord	0.13	0.10	0.02	0.24	1.31	1.25	0.06	0.05
Lung_L	0.18	0.14	0.03	0.23	0.54	0.50	0.04	0.08
Lung_R	0.07	0.05	0.02	0.33	0.14	0.12	0.02	0.18
Stomach	0.05	0.03	0.02	0.67	0.12	0.08	0.05	0.58
Liver	0.03	0.02	0.01	0.61	0.06	0.04	0.02	0.55
Rectum	0.03	0.01	0.01	0.95	0.04	0.02	0.02	1.07
Bladder	0.03	0.01	0.01	1.03	0.06	0.02	0.04	1.69

Abbreviations: OAR, organ-at-risk; EQD2, equivalent doses in 2 Gy fractions.

the simulation. This is because the Au samples were attached near the gap between the collimator and the wall, as shown in Figure 1, and neutrons might have leaked through the gap. Therefore, this gap should be filled with a neutron-shielding material such as LiF-PE. The reaction rates temporarily increased at 70 cm from the irradiation center of the irradiated field (same as the report by Kato et al.[19]), and thereafter, they decreased with a difference less than one digit between measurement and simulation. At a distance of 60–70 cm from the irradiation center, the neutron-shielding materials were changed from LiF-PE to concrete. The difference in the neutron reaction rates that were 70 cm from the irradiation center possibly existed because the details of the concrete composition are unknown; however, the LiF-PE composition was identified. Moreover, the modeled sources had a maximum radius of 150 cm, and the neutrons generated farther from 150 cm possibly contributed to the increase in the experimental reaction rates. This contribution might also have increased the experimental reaction rates on the left, right, and opposite sides of the concrete walls. However, from the perspective of the whole-body dosimetry, the evaluation is insignificantly affected because the head-to-waist areas, where the OARs exist, are within 60 cm from the irradiation center.

The total uncertainties in mixed n/γ irradiation fields are as follows: 5%–7% for the thermal neutron flux, 15%–20% for fast neutrons, and up to 20% for γ-ray dose rates with TLD measurements.[20] This uncertainty includes the setup error of the water phantom and activation samples, which is presupposed as the exact arrangements in QA/QC measurements. Thus, it is difficult to setup the whole-body phantom in a validation with high precision (~1 mm) as a normal QA/QC measurement, which exceeds several centimeters in certain cases because the validation requires arrangements of multiple water tanks in complex combinations and multiple activation samples in parallel. This large setup errors may lead to discrepancies between certain experimental and simulation results, such as Au sample at colon in sitting position as shown in Figure 6. The ability to accurately measure the distribution of the respective reaction and γ-ray dose rates in the rigorous setup is supported by Appendix B and our previous studies.[11] Moreover, the fast neutron flux obtained in the measurements tends to fluctuate, because it is relatively small in this BNCT system, particularly, in the out-of-field region. For Au+Cd, experimental values may have been higher because Au protruding from the Cd reacted with thermal neutrons due to using same diameter of Au and Cd foils. This might be a reason of the phenomena observed at thyroid and bladder points in the sitting position. The largest discrepancy in the ratio of sitting to lying position was seen in the reaction rates of Au, Au+Cd at the breast point, which exceeded 10. The breast point in the sitting position was in close contact with the collimator wall. On the other hand, the point in the lying position was located at a distance from the collimator surface above the phantom. Therefore, the difference in distance is considered to have increased the ratio.

The DVHs as well as $D_{50\%}$ and $D_{2\%}$ of the OAR dose were evaluated using the S_{150} and S_{30} sources. The ε_r value increased as the distance from the irradiation center increased, suggesting that the size (i.e. reproducibility) of the source affects the results. EQD2 of left salivary gland for both S_{150} and S_{30} are sufficiently smaller than one of the dose constraints, $V_{30Gy} < 50\%$ for the parotid gland. This is owing to the advantage that BNCT can suppress the dose to normal tissues. Conversely, the current BNCT is frequently performed for patients with recurrent diseases. Considering dose summation with the irradiation history (x-ray and/or other particle therapy), the dose leaked from the out-of-field region may cause the sum dose to exceed the dose constraints. Clinicians and medical physicists should know that the out-of-field dose increases the OAR dose in the whole-body region. This problem has also been raised in x-ray therapy.[10] Finally, the RBE doses for OARs were compared with those from other studies that investigated irradiation to the head-and-neck region (not EQD2, following the literatures). Different parameters (accelerator equipment, human phantom, detailed setup and beam direction, boron concentration in blood, and irradiation time, etc.) have been used in different studies. Although a straightforward comparison is unavailable owing to the different treatment conditions, the doses evaluated in this study were not significantly different from those of other previous studies. The doses discussed above were "external exposures". The "internal

TABLE 2 Comparison between the OAR doses in the RBE-weighted dose obtained in the current and existing studies.

Author	Herrera et al.	Takada et al.	Postuma et al.	This study	
Dose metric	D_{mean}	D_{mean}	Undescribed	$D_{50\%}$	$D_{2\%}$
^{10}B concentration in blood (ppm)	19.6	24.0	15.0	25.0	25.0
Irradiation time (min) (or dose prescription)	60.0	Time for which skin dose <15 Gy-eq	24.5 min	60.0	60.0
Brain	1.86	–	2.03	0.90	2.95
Eye_L	–	–	–	1.30	1.75
Eye_R	–	–	–	0.44	0.78
Salivary_gland_L	–	–	–	2.91	3.54
Salivary_gland_R	–	–	–	0.46	2.12
Thyroid	3.10	1.16	0.68	0.64	1.50
Esophagus	–	–	–	0.21	1.33
Spinal_cord	–	0.34	–	0.20	1.46
Lung_L	0.14	0.36	0.18 (Lungs)	0.27	0.73
Lung_R	0.18	0.33	0.18 (Lungs)	0.11	0.22
Stomach	0.04	–	0.22	0.08	0.19
Liver	0.08	0.12	0.34	0.05	0.09
Rectum	–	–	–	0.05	0.07
Bladder	–	–	0.09	0.05	0.09

Abbreviations: OAR, organ-at-risk; RBE, relative biological effectiveness.

exposure" due to radionuclides generated in the body during BNCT should have been evaluated separately. The internal doses evaluated in this study were approximately 10^6 times smaller than the external doses, and they can be neglected in the dose assessment.

The limitations of this study were as follows: First, only one experiment was possible for each validation because of the machine time constraints. The discrepancies between experimental and simulation results at several points in the validation using the human-body phantom is expected to decrease with performing the experiments multiple times. Second, the OAR doses were evaluated in only one relatively simple supine position. In clinical BNCT, various positioning techniques are applied for each patient to position affected areas as close as possible to the collimator hole.[21] Recently, extended collimators designed and validated by our group have relatively simplified the patient setup and allow the patient to be in the supine position, particularly, in the earcanal region.[22] However, even now, complex sitting and lying postures are often performed, and whole-body doses may be different for each patient. For this reason, a dose evaluation system for individual patient setups should be established in future. To achieve this, dose evaluation in different postures by utilizing the deformability of the mesh phantom is expected to be useful. Third, fixed RBE and CBE factors were used to evaluate the total dose. Recently, other calculation models such as the photon-isoeffective dose are suggested, which may output a different total dose. Fourth, our study focused on the out-of-field dosimetry in the current BNCT system. Based on this study, more optimal neutron shielding materials and design will be an important research to improve the safety of BNCT.

5 | CONCLUSIONS

The PHITS model used for clinical BNCT of the whole-body region was validated, and then the OAR doses were evaluated. The experimental and simulation results of reaction rates of Au samples for the whole-room validation conducted in the whole-body region were almost in good agreement. The reaction and γ-ray dose rates of both the couch and chair in whole-body phantom validations agreed well within the experimental uncertainty, except several measured points. Extending the PHITS model to the whole-body region resulted in higher doses for all OARs, especially 0.13 increase of ε_a for $D_{50\%}$ of left salivary gland. Clinicians and medical physicists should know that the out-of-field radiation increases the OAR dose in the whole-body region.

ACKNOWLEDGMENTS

The authors are grateful to all the Kansai BNCT Medical Center staff, Osaka Medical and Pharmaceutical University (https://www.ompu.ac.jp/kbmc/), for their valuable comments and discussions, and to Sumitomo Heavy Industries, Ltd. for their assistance with the Monte Carlo beam-modeling process. Moreover, we extend our

gratitude to Editage (www.editage.com) for English language editing. This research was supported in part by the Japan Society for the Promotion of Science (JSPS) Grant-in-Aid for Research Activity Start-up (grant number 21K20521) and JSPS Grant-in-Aid for Scientific Research (Grant Number 21K15793).

CONFLICT OF INTEREST STATEMENT

The authors have no conflicts of interest to disclose.

REFERENCES

1. Tanaka H, Sakurai Y, Suzuki M, et al. Characteristics comparison between a cyclotron-based neutron source and KUR-HWNIF for boron neutron capture therapy. *Nucl Instrum Methods Phys Res, Sect B*. 2009;267(11):1970-1977.
2. Tanaka H, Sakurai Y, Suzuki M, et al. Experimental verification of beam characteristics for cyclotron-based epithermal neutron source (C-BENS). *Appl Radiat Isot*. 2011;69(12):1642-1645.
3. Sumitomo Heavy Industries L., BNCT System NeuCure®, Accessed 26 December, 2022, https://www.shi.co.jp/industrial/en/product/medical/bnct/neucure.html
4. Hirose K, Konno A, Hiratsuka J, et al. Boron neutron capture therapy using cyclotron-based epithermal neutron source and borofalan (10B) for recurrent or locally advanced head and neck cancer (JHN002): an open-label phase II trial. *Radiother Oncol*. 2021;155:182-187.
5. Imoto M, Tanaka H, Fujita K, et al. Evaluation for activities of component of Cyclotron-Based Epithermal Neutron Source (C-BENS) and the surface of concrete wall in irradiation room. *Appl Radiat Isot*. 2011;69(12):1646-1648.
6. Tsukamoto T, Tanaka H, Yoshinaga H, et al. A phantom experiment for the evaluation of whole body exposure during BNCT using cyclotron-based epithermal neutron source (C-BENS). *Appl Radiat Isot*. 2011;69(12):1830-1833.
7. Herrera MS, González SJ, Minsky DM, Kreiner AJ. Evaluation of performance of an accelerator-based BNCT facility for the treatment of different tumor targets. *Physica Med*. 2013;29(5):436-446.
8. Takada K, Kumada H, Isobe T, et al. Whole-body dose evaluation with an adaptive treatment planning system for boron neutron capture therapy. *Radiat Prot Dosim*. 2015;167(4):584-590.
9. Postuma I, González S, Herrera MS, et al. A novel approach to design and evaluate BNCT neutron beams combining physical, radiobiological, and dosimetric figures of merit. *Biology*. 2021;10(3). doi:10.3390/biology10030174
10. Kry SF, Bednarz B, Howell RM, et al. AAPM TG 158: measurement and calculation of doses outside the treated volume from external-beam radiation therapy. *Med Phys*. 2017;44(10):e391-e429.
11. Hu N, Tanaka H, Kakino R, et al. Evaluation of a treatment planning system developed for clinical boron neutron capture therapy and validation against an independent Monte Carlo dose calculation system. *Radiat Oncol*. 2021;16(1):243.
12. Sato T, Iwamoto Y, Hashimoto S, et al. Features of Particle and Heavy Ion Transport code System (PHITS) version 3.02. *J Nucl Sci Technol*. 2018;55(6):684-690.
13. Sakurai Y, Kobayashi T. Characteristics of the KUR heavy water neutron irradiation facility as a neutron irradiation field with variable energy spectra. *Nucl Instrum Methods Phys Res A*. 2000;453(3):569-596.
14. Cai D, Yu B, Lu H, Zhao W. *Evaluation of the 115In(n,n') 115mIn Reaction Cross Section*. International Atomic Energy Agency (IAEA); 1991.
15. Hu N, Tanaka H, Akita K, et al. Accelerator based epithermal neutron source for clinical boron neutron capture therapy. *J Neutron Res*. 2022;24:359-366.
16. Firestone RB. Nuclear data sheets for A = 24. *Nucl Data Sheets*. 2007;108(11):2319-2392.
17. Blachot J. Nuclear data sheets for A = 115. *Nucl Data Sheets*. 2012;113(10):2391-2535.
18. Prescribing, recording, and reporting photon-beam intensity-modulated radiation therapy (IMRT). ICRU Report 83. *J ICRU*. 2010;10(1):1-106.
19. Kato T, Hirose K, Tanaka H, et al. Design and construction of an accelerator-based boron neutron capture therapy (AB-BNCT) facility with multiple treatment rooms at the Southern Tohoku BNCT Research Center. *Appl Radiat Isot*. 2020;156:108961.
20. International Atomic Energy Agency. *Current Status of Neutron Capture Therapy*. International Atomic Energy Agency; 2001.
21. Komori S, Hirose K, Sato M, et al. Dosimetric effect of set-up error in accelerator-based boron neutron capture therapy for head and neck cancer. *J Radiat Res (Tokyo)*. 2022;63(4):684-695.
22. Hu N, Tanaka H, Kakino R, et al. Improvement in the neutron beam collimation for application in boron neutron capture therapy of the head and neck region. *Sci Rep*. 2022;12(1):13778.
23. Knezevic J, Mrdja D, Hansman J, et al. Corrections of HPGe detector efficiency curve due to true coincidence summing by program EFFTRAN and by Monte Carlo simulations. *Appl Radiat Isot*. 2022;189:110421.
24. Nakamura S, Wakita A, Ito M, et al. Modeling the detection efficiency of an HP-Ge detector for use in boron neutron capture therapy. *Appl Radiat Isot*. 2017;125:80-85.
25. Hingu A, Soni B, Parashari S, et al. Cross-sections for production of In115m by quasi-monoenergetic neutrons within 7–20 MeV. *Radiat Phys Chem*. 2022;199:110270.
26. Kumada H, Takada K. Treatment planning system and patient positioning for boron neutron capture therapy. *Ther Radiol Oncol*. 2018;2:50.
27. Eckerman K, Harrison J, Menzel H-G, Clement CH. ICRP publication 119: compendium of dose coefficients based on ICRP publication 60. *Ann ICRP*. 2013;42(4):1-130.

How to cite this article: Kakino R, Hu N, Tanaka H, et al. Out-of-field dosimetry using a validated PHITS model and computational phantom in clinical BNCT. *Med Phys*. 2024;51:1351–1363. https://doi.org/10.1002/mp.16916

APPENDIX A: ACTIVATION METHOD AND THE HPGE DETECTION EFFICIENCY

As the irradiation field of accelerator-based BNCT is a neutron-gamma mixed-filed activation method, which is an indirect neutron measurement, it is frequently used to discriminate neutrons from γ-rays. The reaction rate per atom per coulomb R [C^{-1}atom^{-1}] is expressed as

$$R = \frac{\lambda C\left(\frac{t_r}{t_c}\right)}{N_0 \varepsilon \gamma e^{-\lambda T_C}\left(1-e^{-\lambda T_m}\right)\sum_{i=1}^{n}\left(\frac{Q_i}{\Delta t}\left(1-e^{-\lambda \Delta t}\right)e^{-\lambda(n-i)\Delta t}\right)}, \tag{A1}$$

where the coefficients are summarized in Table A1. The detection efficiency ε of the HPGe detector in Equation (A1) was evaluated via both an experiment and a simulation. The experiment was performed

TABLE A1 Parameters and their expressions for evaluating reaction rate R in the activation method.

Parameter	Expression
λ	Decay constant [s^{-1}]
C	Peak count
t_c	Counting time [s]
t_r	Real time (clock time) [s]
N_0	Number of target nuclei in the sample
ε	Detection efficiency of the HPGe detector
γ	γ-ray emission rate
T_c	Time from the irradiation to the start of measurements [s]
T_m	Measurement time [s]
Q_i	Electric charge irradiated on target at each interval Δt [C]

TABLE A2 Radionuclides and their photon energy inside the standard source.

Radionuclide	Photon energy (keV)
^{109}Cd	88.0
^{57}Co	122.1
^{139}Ce	165.9
^{203}Hg	279.2
^{113}Sn	391.7
^{85}Sr	514.0
^{137}Cs	661.6
^{88}Y	898.0, 1836.0
^{60}Co	1173.0, 1333.0

using radioactive standard sources (Japan Radioisotope Association), capsuling nine radioisotopes, as summarized in Table A2. The pulse-height spectrum was measured and the ε values for each γ-ray peak were evaluated. Conversely, the HPGe detector system and γ-ray sources were modeled in the simulation based on the blueprint. [T-deposit] function was used to evaluate energy deposition inside the HPGe detector and the ε values for each radionuclide. For ^{88}Y and ^{60}Co, the ε values considering true coincidence summing (TCS) due to the simultaneous emission of two γ-rays[23] were evaluated using the "iscorr" parameter. After the validation, the ε values of the activation samples used in this study were evaluated in the simulation. For the Al samples, TCS correction (TCSC) was also considered because of simultaneous the two-γ-ray emission from ^{24}Na.[16]

Figure A1 shows the ε values as a function of the γ-ray energy for both the experiment and simulation. The ε values from the simulation agreed well with those from the experiment except for 88.0, 165.9, 898.0, 1173.0, 1333.0, and 1836.0 keV. The disagreements in 88 and 165.9 keV could be improved by optimizing the thickness of the outer dead layer of the HPGe detector, as reported by Nakamura et al.[24] As γ-rays below 336 keV were not utilized in this study; therefore, the HPGe model will be optimized in future work. The disagreements in 898.0, 1173.0, 1333.0, and 1836.0 keV were improved by considering the TCSC.

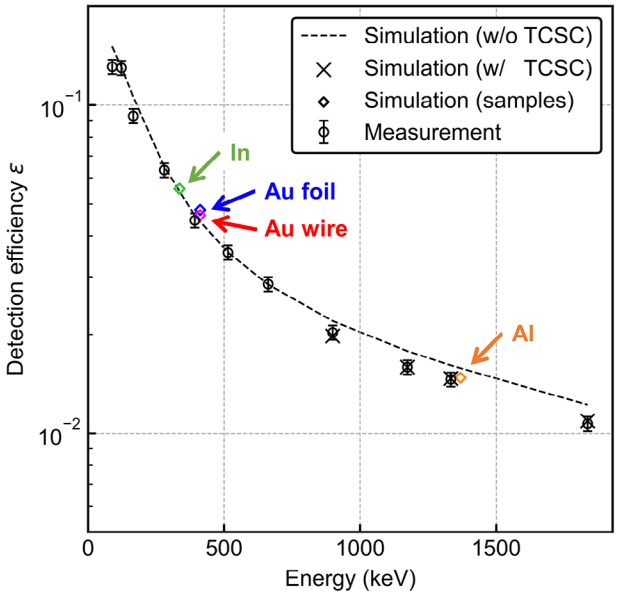

FIGURE A1 Detection efficiency as a function of γ-ray energy. TCSC, true coincidence summing correction.

APPENDIX B: VALIDATION OF FAST NEUTRONS

Fast neutrons inside the water phantom were validated via reaction rates of In and Al foils used in the main section. ^{115}In(n, n')^{115m}In and ^{27}Al(n, α)^{24}Na reactions were quantified. The measuring points were 0, 1, 2, and 6 cm in the depth direction, and 3 and 6 cm in the off-axis direction, as shown in Figure B1. The samples

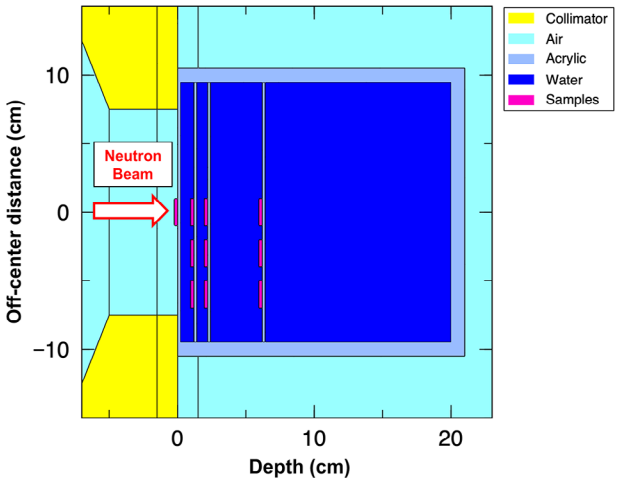

FIGURE B1 Arrangement of the water phantom and In or Al samples for the fast neutron detection.

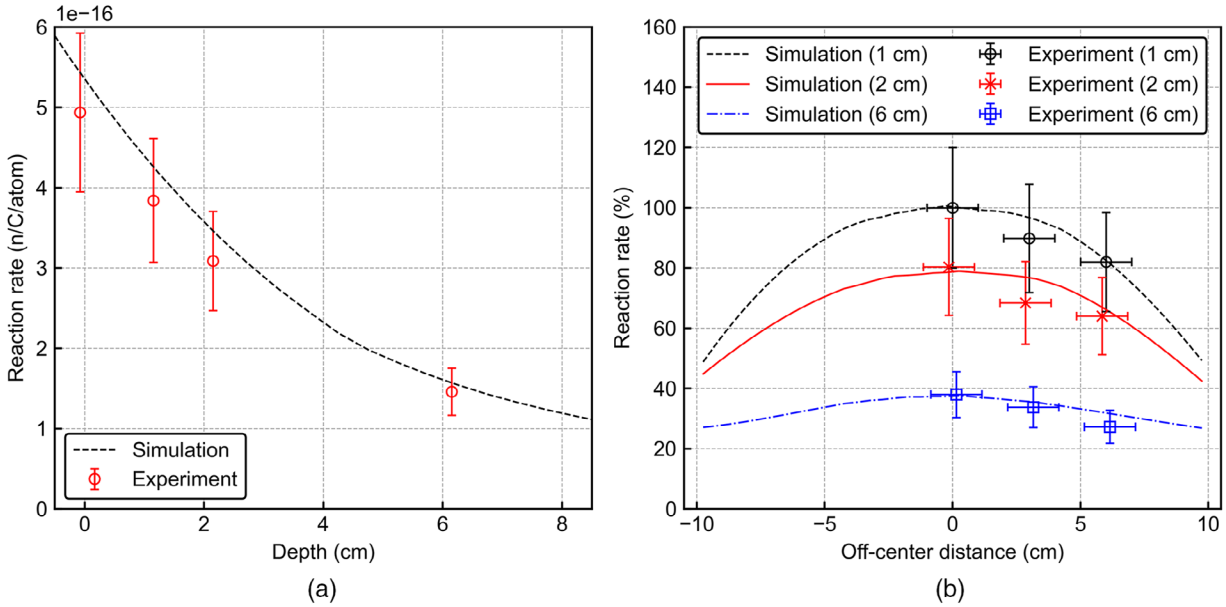

FIGURE B2 (a) DR and (b) OCR measured by In samples. DR, depth reaction rate; OCR, off-center ratio.

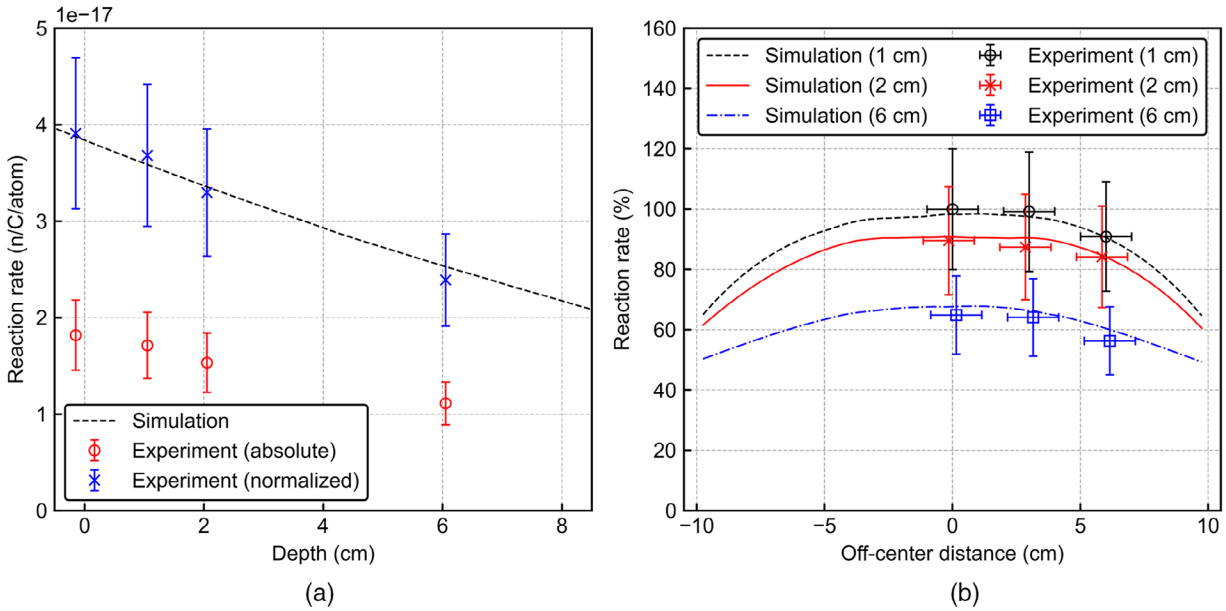

FIGURE B3 (a) DR and (b) OCR measured by Al samples. The DR was normalized at surface point by a factor of 2.15. DR, depth reaction rate; OCR, off-center ratio.

were covered by Cd to avoid the unnecessary activation with thermal neutrons. Total proton charges of 3.6 C were delivered. After the irradiation, 336 or 1369 keV γ-rays emitted from the activated ^{115m}In or ^{24}Na samples, respectively, were measured with the HPGe detector. The measured counts were converted to the reaction rate per unit charge of the In or Al samples, based on Equation (4). The detection efficiency was referred from Appendix A. The simulation procedure was the same as that discussed in the main section. For the simulation of In sample activation, the cross section of the ^{115}In(n, n')^{115m}In reaction was referred from Hingu et al.,[25] which had been experimentally summarized.

Figures B2 and B3 shows the depth reaction rate (DR) and off-center ratios (OCRs) of the In or Al samples. For the In samples, the reaction rates observed in the experiment were slightly lower than those observed in the simulation, but they agreed within experimental uncertainty (maximum difference in DR was 8.1%). For the Al samples, the reaction rates of the experiment

were significantly lower than those of the simulation (maximum difference in DR was 55.2%). Multiplying the experimental value by 2.15 produced a good agreement with the simulation value (3.6% difference). This is possibly because the neutron spectrum of above 3.4 MeV in the simulation closely agreed with of the experiment in terms of the spectral shape, but was higher than the actual neutron flux. However, the exact reason is unknown. As a future work, it is desirable to validate fast neutrons in a wider energy range by using activation foils other than In and Al. For the validation in the main section, a relative comparison was performed by multiplying the experimental results by 2.15.

APPENDIX C: BNCT DOSE CALCULATION

The RBE-weighted dose D_T (Gy-eq) for BNCT can be evaluated using Equations (C1) and (C2), and their coefficients are summarized in Table C1[26]:

$$D_n = \int_t \int_E f_n(E)\ \phi(E,\ t)\, dEdt, \tag{C1}$$

$$D_T = CBE \times D_B + RBE_N \times D_N + RBE_H \times D_H + D_\gamma, \tag{C2}$$

TABLE C1 Parameters and their expressions for evaluating the RBE-weighted dose.

Parameter	Expression	Values if defined
D_n	Absorbed dose arising from neutrons and atoms	–
f_n	Kinetic energy released in the matter (KERMA) factors for neutrons	–
Φ	Neutron flux at a given point	–
CBE	Compound biological effectiveness for healthy tissue	1.34
RBE_N	Relative biological effectiveness for nitrogen	2.9
RBE_H	Relative biological effectiveness for hydrogen	2.4
D_B	Dose due to ^{10}B fission reaction (^{10}B (n,α)^{7}Li)	–
D_N	Dose due to ^{14}N capturing a thermal neutron and emitting a proton in the ^{14}C(n,α)^{14}N reaction	–
D_H	Dose due to epithermal and fast neutrons causing reoil protons from hydrogen	–
D_γ	γ-ray dose	–

APPENDIX D: INTERNAL EXPOSURE

Internal doses due to radionuclides produced in the MRCP by the neutron irradiation were evaluated. First, the radioactivity produced in the MRCP was calculated using the [T-deposit] function of PHITS and D-CHAIN version 3.25, with the same geometry as in Figure 4. Then, the radioactivity obtained after the irradiation was converted to the committed effective dose $E(\tau)$ (Sv) using the following equation:

$$E(\tau) = \sum_n e(\tau, n)\, A(n)\ , \tag{D1}$$

where n is the radionuclide, $e(\tau, n)$ (Sv/Bq) is the dose coefficient of radionuclide n for the commitment period of τ years (= 50 years for adults),[27] and $A(n)$ (Bq) is the produced radioactivity of radionuclide n after neutron irradiation. Subsequently, $E(50)$ was 6.50×10^{-6} Sv. The top ten radionuclides with the highest internal doses in the MRCP are summarized in Table D1. Assuming that 1 Sv = 1 Gy-eq, the internal dose was sufficiently lower than the external dose such that it was considered negligible.

TABLE D1 Top ten radionuclides with the highest internal doses in the MRCP.

Radionuclide	Activity [Bq]	Dose coefficients [Sv/Bq]	Doses [Sv] (ratio [%])
^{38}Cl	2.52×10^{4}	1.20×10^{-10}	3.02×10^{-6} [46.48%]
^{24}Na	5.01×10^{3}	4.30×10^{-10}	2.16×10^{-6} [33.15%]
^{42}K	1.33×10^{3}	4.30×10^{-10}	5.72×10^{-7} [8.80%]
^{40}K	6.51×10^{1}	6.20×10^{-9}	4.04×10^{-7} [6.21%]
^{32}P	7.28×10^{1}	3.40×10^{-9}	2.48×10^{-7} [3.81%]
^{35}S	4.54×10^{1}	1.90×10^{-9}	8.63×10^{-8} [1.33%]
^{11}C	2.34×10^{2}	2.40×10^{-11}	5.61×10^{-9} [0.09%]
^{31}Si	3.50×10^{1}	1.60×10^{-10}	5.60×10^{-9} [0.09%]
^{14}C	2.82×10^{-1}	5.80×10^{-9}	1.64×10^{-9} [0.03%]
^{56}Mn	4.43×10^{0}	2.50×10^{-10}	1.11×10^{-9} [0.02%]

Abbreviation: MRCP, mesh-type reference computational phantom.